IEEE Access
Multidisciplinary | Rapid Review | Open Access Journal

Received 8 October 2024, accepted 25 October 2024, date of publication 28 October 2024, date of current version 11 November 2024.

Digital Object Identifier 10.1109/ACCESS.2024.3487351

RESEARCH ARTICLE

Analytical Model of a High-Frequency Rotary Transformer

MANUELE BERTOLUZZO, NICOLA BIANCHI, (Fellow, IEEE), AND FRANCESCO TRIPALDI, (Member, IEEE)
Department of Industrial Engineering, University of Padova, 35131 Padua, Italy

Corresponding author: Manuele Bertoluzzo (manuele.bertoluzzo@unipd.it)

This work was supported in part by the MOST—National Sustainable Mobility Center, and in part by European Union Next-Generation EU (Piano Nazionale di Ripresa e Resilienza (PNRR)—Missione 4 Componente 2, Investimento 1.4—D.D. 1022 17/06/2022) under Grant CN00000023.

ABSTRACT The permanent magnet synchronous motors are widely used for the propulsion of electric vehicles. These motors have good performance, but result expensive because the permanent magnets installed on their rotor contain rare earths. A promising solution to reduce the cost of the motors is to replace the magnets with an excitation coil, which requires to transfer its own supply power to the rotor of the motor. The power transfer is performed by means of a rotary transformer. This paper develops a simplified steady state model of the rotary transformer which allows to asses with good accuracy the position of some points in the waveforms of the currents in the primary and secondary coils of the transformer and in the excitation coil. The inputs of the model are the inductive parameters of the transformer itself and the electrical parameters of the power switches that compose the inverter that supplies the primary coil and of the diodes that form the rectifier connected to the secondary coil. The accuracy of the analytical expressions that give the position of the points on the current waveforms is verified by comparison with the results obtained from simulations and with the current waveforms acquired from a prototypal transformer available in the lab.

INDEX TERMS Rotary transformer, analytical model, excitation coil.

I. INTRODUCTION

It is common opinion that a wider use of electric vehicles (EVs) can reduce polluting emissions and delay the depletion of fossil fuels. The electric motor is one of the most important components of EVs. It must provide high starting torque, operate over a wide speed range, offer high efficiency and simplicity of control. In the past, dc motors have been used; currently, induction motors, switched reluctance motors and permanent magnet motors are installed on EVs [1]. The latter offer the best performance in terms of power density, specific power and efficiency [2]. Unfortunately, their cost has recently increased due to the use of rare earths in the production of magnets and therefore studies have been undertaken to evaluate the possibility of reducing the quantity of magnets needed in each motor. A promising solution is to use excitation coils instead of magnets to create the rotor magnetic field. The motors that implement this solution are often denoted as electrically excited synchronous motors (EESMs). Different aspects have been considered in [3] to optimize the design of the EESMs. In [4] the excitation system of the EESM encompasses a small asynchronous exciter and a rotating three-phase diode bridge rectifier. In [5] a brushless EESM having a rotor with slots similar to those of a synchronous reluctance machine is considered.

The excitation coil could be powered by means of brushes, but they are subject to wear and require periodic maintenance. Paper [6] presents a radical solution to this problem by proposing a motor with a winding-free rotor and a stator that has both excitation and power windings. Another particular solution is presented in [7], where an EESM with one set of stator windings and two set of rotor windings is considered. A component of the stator flux rotates asynchronously to the rotor and induce a voltage across one of the rotor windings set. The consequent current is rectified and used to supply the other rotor winding set that generates the magnetic field.

The associate editor coordinating the review of this manuscript and approving it for publication was Paolo Giangrande.

However, the approach most often considered in the literature to get rid of brushes and rings relies on a wireless power transfer system built around a high frequency rotary transformer (HFRT). In [8] a model comprehensive of the motor and of the HFRT coil is presented. In studying the HFRT different aspects should be considered, such as the coils layout [9], the losses and thermal effects [10], the overall system modeling [11]. This paper is focused on this last aspect and aims at developing closed form formulas that describe the steady state behavior of the HFRT and of the excitation coil. More in details, the obtained formulas give the time instants of the occurrence of particular points in the current waveforms and the corresponding values of the instantaneous current. Given the waveform of the currents considered in this application, the knowledge of the pairs of time-current values in these key points allows to completely reconstruct the entire current waveform during a supply period. To achieve this result, the paper performs a detailed analysis of the functioning of a HFRT operating at steady state. The analysis is carried out following the approach of predicting the system operation rather than explaining the results obtained from a prototype or by simulation. This approach leads to a deeper understanding of the system behavior and allows to make apart the aspects of its functioning intrinsic to its structure from those which instead depend on the particular implementation under consideration.

In performing the analysis, some simplifications have been introduced to obtain workable expressions of the amplitudes of the currents at the key points. Beside illustrating the functioning of the system, these expressions could give useful hints about the sizing of the transformer, of the excitation coil, of the rectifier and of the supply high frequency inverter (HFI). Moreover, they can be used to assess the effects of the variations of one or more parameters of the rotary transformer on the amplitudes of the currents. The analysis method proposed in this paper has been applied to a prototypal HFRT whose electromechanical parameters are known. The accuracy of the obtained results has been verified by comparing them with the outcomes both of simulations and of experimental tests performed on the prototype.

The paper is organized as follows. Section II gives a detailed description of the overall system, considering the parasitic effects of its components and analyzing the functioning of the diode rectifier in different working conditions along one supply period. Section III develops the equations that express the currents behavior as a function of the supply voltage, of the parameters of the rotary transformer and of the excitation coil, of their parasitic element and of those of the supply inverter and of the rectifier. Section IV finds approximate solutions of the equations developed in Section III to work out the analytical expressions for the amplitudes of the currents at the key points and a description of their waveforms. Section V compares the analytical result with those coming from simulations. Section VI compares the analytical results with the outcomes of experimental tests performed on a prototype. Section VII concludes the paper.

II. CIRCUIT ANALYSIS

The simplified scheme of the circuit for the high frequency inductive supply of the excitation coil is sketched in Fig. 1.

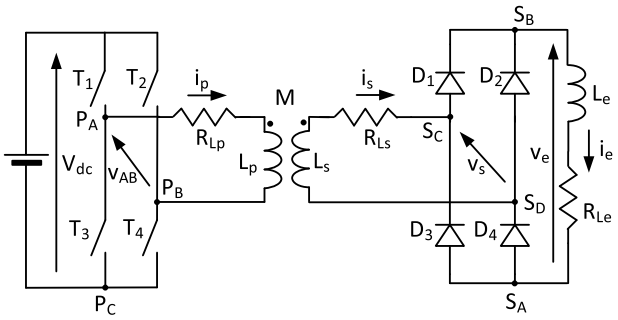

FIGURE 1. Schematic of the high frequency inductive supply.

The element that characterizes the system is the HFRT. It is modeled by the self-inductances L_p and L_s and the parasitic resistances R_{Lp} and R_{Ls} of its primary and secondary coils and by their mutual inductance M.

The current i_p, supplied by the HFI, flows in the primary coil. The HFI is formed by the four MOSFET T_1, T_2, T_3, and T_4 arranged in a H-bridge and controlled by the phase shift technique. The dc side of the HFI is supplied by the constant voltage V_{dc}. The secondary coil is connected to a full-wave diode rectifier (DR) formed by the diodes D_1, D_2, D_3, and D_4. The dc side of the DR supplies the excitation coil, modeled by its self-inductance L_e and its resistance R_e.

This is the most common solution found in the literature, even if other layouts can be implemented, for example based on a three-phase transformer [12] or on a single-phase transformer with a center-tap secondary coil connected to a two-diodes rectifier [13].

A. HIGH FREQUENCY INVERTER OPERATIONS

Given the high frequency of the supply voltage, some authors analyze the behavior of the HFRT considering only the first harmonic of the involved currents and voltages [14], [15]. This paper, instead, considers the real waveform the supply voltage. According to the phase shift technique, the switching commands of transistors T_1 and T_3 are complementary square waves with duty cycle equal to 50% and switching period T. The switching commands of T_2 and T_4 have the same waveform but are shifted of the phase angle φ. In the hypothesis that the on-resistances R_T of the transistors are equal to zero, the voltages of the nodes P_A and P_B with respect to P_C are square waves with amplitude V_{dc} and shifted one with respect to the other of the phase angle φ, corresponding to a time delay of δT, as shown in the upper and in the middle plots of Fig. 2. The supply voltage v_{AB} of the primary coil is given by the difference v_{AC}-v_{BC} and is shown in the lower plot of Fig. 2. It is a quasi-square wave having period T, equal to the switching period of the HFI, and duty cycle given by

$$\delta = \frac{\phi}{2\pi}. \tag{1}$$

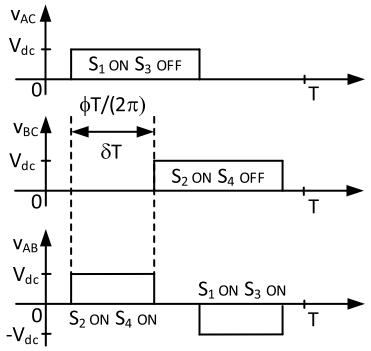

FIGURE 2. Voltages relevant to the phase shift technique.

A more accurate model of the transistors should consider their on-resistances R_T. According to the scheme of Fig. 1 and to the HFI operations described above, two of these resistances are always connected in series to the primary coil. Consequently, looking upstream from the nodes P_A and P_B to the HFI output, the primary side of the system can be modeled with the equivalent scheme of Fig. 3, where the HFI is formed by the ideal transistors IT_x and the on-resistances are connected in series to the primary coil. The supply voltage v_p generated by the ideal HFI takes the values V_{dc}, 0, or $-V_{dc}$ according to the switching commands of the transistors and satisfies the relation

$$v_p = R_{p,eq} i_p + L_p \frac{di_p}{dt} - M \frac{di_s}{dt}, \tag{2}$$

where $R_{p,eq}$ is defined as

$$R_{p,eq} \triangleq 2R_T + R_{Lp}. \tag{3}$$

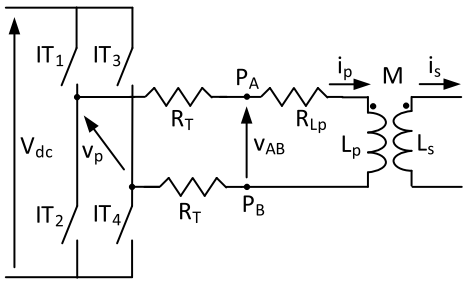

FIGURE 3. Equivalent scheme of the high frequency inverter.

B. DIODE RECTIFIER OPERATIONS

Analysis of the DR functioning is performed with the help of Fig. 4, which models the four diodes of Fig. 1 as the series of an ideal diode ID_x and of its on-resistance R_{Dx} and forward voltage V_{Dx}.

From the simple consideration that a positive i_s flows through D_1 and that in the node S_B it sums to any current flowing through D_2 to originate the excitation current i_e, it derives that $i_s \leq i_e$. A symmetrical result is obtained when $i_s < 0$, so that it comes that in any operating condition

$$|i_s| \leq i_e. \tag{4}$$

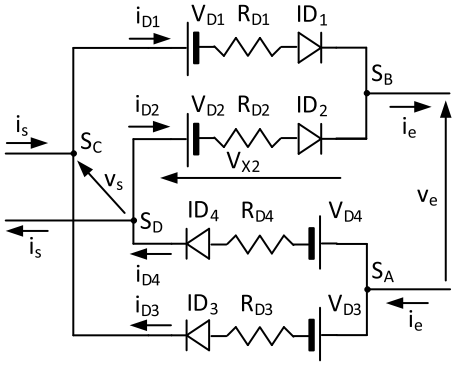

FIGURE 4. Equivalent circuit of the diode rectifier.

Moreover, in the nodes S_C and S_D, the currents satisfy

$$\begin{aligned} i_s &= i_{D1} - i_{D3} \\ i_s &= i_{D4} - i_{D2}, \end{aligned} \tag{5}$$

whilst for the nodes S_A and S_B it is

$$\begin{aligned} i_e &= i_{D1} + i_{D2} \\ i_e &= i_{D3} + i_{D4} \end{aligned} \tag{6}$$

The two voltages v_s and v_e are linked through the DR and their actual relation depends on the conduction condition of the four diodes ID_1-ID_4 that, in turn, changes according to the instantaneous amplitude of the current i_s with respect to i_e. In any case, from Fig. 1 it can be immediately recognized that

$$v_s = -R_{Ls} i_s - L_s \frac{di_s}{dt} + M \frac{di_p}{dt} \tag{7}$$

$$v_e = R_e i_e + L_e \frac{di_e}{dt}. \tag{8}$$

1) RECTIFIER OPERATIONS WITH $|i_s| = i_e$

If $i_s = i_e$, from the first of (5) and (6) it derives that $i_{D2} = -i_{D3}$.

However, the currents in the diodes must be positive, hence it comes that if $i_s = i_e$, then $i_{D3} = i_{D2} = 0$ and the current flows only through diodes D_1 and D_4.

In this condition, from the analysis of the circuit of Fig. 4 it comes that

$$v_s = R_{D4} i_s + V_{D4} + v_e + R_{D1} i_s + V_{D1}. \tag{9}$$

In (9) and in some of the following equations, different subscripts have been used for the on-resistances and the forward voltages of the diodes in order to make easier recognizing the path followed in Fig. 4 to compute the voltage drops. Nevertheless, the analysis of the system is simplified by considering the same value R_D for all the R_{Dx} and the same V_D for all the V_{Dx}. Thus, (9) simplifies into

$$v_s = 2R_D i_s + 2V_D + v_e, \tag{10}$$

i.e. v_s must be high enough to compensate for the voltage drops across the conducting diodes D_1 and D_4 and to force i_e to flow across R_e and L_e.

By substituting (7) and (8) in (10) and by remembering that the latter one holds for $i_s = i_e$, the following relation is obtained

$$2V_D = -(R_{Ls} + 2R_D + R_e)\, i_s - (L_s + L_e)\frac{di_s}{dt} + M\frac{di_p}{dt}. \tag{11}$$

Manipulation of (2) and (11) leads to the expressions of the rates of the primary and secondary currents that hold when $i_s = i_e$:

$$\frac{di_p}{dt} = \frac{1}{1-k_{eq}^2}\frac{1}{L_p}\left(v_p - R_{p,eq}i_p\right) - \frac{k_{eq}^2}{1-k_{eq}^2}\frac{1}{M}\left(2V_D + R_{s,eq}i_s\right) \tag{12}$$

$$\frac{di_s}{dt} = \frac{k_{eq}^2}{1-k_{eq}^2}\frac{1}{M}\left(v_p - R_{p,eq}i_p\right) - \frac{1}{1-k_{eq}^2}\frac{1}{L_{s,eq}}\left(2V_D + R_{s,eq}i_s\right), \tag{13}$$

where $R_{s,eq}$ and $L_{s,eq}$ are defined as

$$R_{s,eq} \triangleq R_{Ls} + 2R_D + R_e, \quad L_{s,eq} \triangleq L_s + L_e, \tag{14}$$

and k_{eq}^2 is

$$k_{eq}^2 \triangleq \frac{M^2}{L_p L_{s,eq}} = \frac{L_s}{L_{s,eq}}k^2. \tag{15}$$

By substituting back (12) and (13) in (7) and considering the definition (15), the following expression of v_s is obtained:

$$v_s = -R_{Ls}i_s + \frac{M}{L_p}\left(1 - \frac{k_{eq}^2}{k^2}\right)\left(\frac{1}{1-k_{eq}^2}\right)\left(v_p - R_{p,eq}i_p\right) + \frac{L_s}{L_{s,eq}}\left(\frac{1-k^2}{1-k_{eq}^2}\right)\left(2V_D + R_{s,eq}i_s\right). \tag{16}$$

On the contrary, if $i_s = -i_e$, the conducting diodes are D_2 and D_3 and v_s is

$$v_s = 2R_D i_s - 2V_D - v_e. \tag{17}$$

Substitution of (7) and (8) in (17) leads to

$$2V_D = R_{s,eq}i_s + L_{s,eq}\frac{di_s}{dt} - M\frac{di_p}{dt}. \tag{18}$$

Manipulation of (2) and (18) leads to the expressions of the rates of the primary and secondary currents that hold when $i_s = -i_e$:

$$\frac{di_p}{dt} = \frac{1}{1-k_{eq}^2}\frac{1}{L_p}\left(v_p - R_{p,eq}i_p\right) - \frac{k_{eq}^2}{1-k_{eq}^2}\frac{1}{M}\left(-2V_D + R_{s,eq}i_s\right) \tag{19}$$

$$\frac{di_s}{dt} = \frac{k_{eq}^2}{1-k_{eq}^2}\frac{1}{M}\left(v_p - R_{p,eq}i_p\right) - \frac{1}{1-k_{eq}^2}\frac{1}{L_{s,eq}}\left(-2V_D + R_{s,eq}i_s\right). \tag{20}$$

On its turn, (16) changes into (21)

$$v_s = -R_{Ls}i_s + \frac{M}{L_p}\left(1 - \frac{k_{eq}^2}{k^2}\right)\left(\frac{1}{1-k_{eq}^2}\right)\left(v_p - R_{p,eq}i_p\right) + \frac{L_s}{L_{s,eq}}\left(\frac{1-k^2}{1-k_{eq}^2}\right)\left(-2V_D + R_{s,eq}i_s\right). \tag{21}$$

About the rate of i_e, obviously it is

$$\frac{di_e}{dt} = \pm\frac{di_s}{dt}, \tag{22}$$

with the + or − sign according to the sign of i_s.

2) RECTIFIER OPERATIONS WITH $|i_s| < i_e$

If $i_e > i_s > 0$, at a first glance it could be supposed to have three conducting diodes, for example D_1, D_2, and D_3 carrying the currents i_e, i_e-i_s, and i_s, respectively. In this condition, the voltage v_e, computed across the D_1, D_3 pair or the D_2, D_4 pair, can be expressed in two different ways as

$$\begin{aligned} v_e &= -V_{D3} - R_{D3}(i_e - i_s) - V_{D1} - R_{D1}i_e \\ v_e &= -V_{D4} - R_{D4}i_s - V_{X2}, \end{aligned} \tag{23}$$

where V_{X2}, highlighted in Fig. 4, is the voltage across the diode D_2, which is assumed not to conduct. Equating the two expressions of v_e, V_{X2} results

$$V_{X2} = V_D + 2R_D(i_e - i_s). \tag{24}$$

Hence, the diode D_2 is directly polarized and should be in conduction state. Consequently, the hypothesis of having only three conducting diodes is wrong and, instead, all the four diodes are in conduction state.

Then, (23) can be rewritten as

$$\begin{aligned} v_e &= -V_{D3} - R_{D3}i_{D3} - V_{D1} - R_{D1}i_{D1} \\ v_e &= -V_{D4} - R_{D4}i_{D4} - V_{D2} - R_{D2}i_{D2}, \end{aligned} \tag{25}$$

and equating the two expressions of v_e the following relation is obtained

$$i_{D3} + i_{D1} = i_{D4} + i_{D2}. \tag{26}$$

By manipulating (26) and (6), it derives that

$$i_{D1} = i_{D4}, \tag{27}$$

$$i_{D2} = i_{D3}. \tag{28}$$

By substitution of (28) in the first of (25) and considering (6), relation (29) is obtained

$$v_e = -2V_D - R_D i_e. \tag{29}$$

The voltage v_s results as the sum of the voltage drops across D_4 and D_3 and is given by

$$v_s = (R_{D4}i_{D4} + V_{D4}) - (V_{D3} + R_{D3}i_{D3}) = R_D i_s, \tag{30}$$

where the last equality has been obtained by using (27) and the first of (5). By comparison with (10), it comes that now v_s is lower than the voltage needed to have two conducting diodes. Indeed, if the diodes resistance is neglected, the secondary coils can be considered short-circuited.

Substitution of (7) in (30) leads to

$$0 = -(R_{Ls} + R_D)\, i_s - L_s \frac{di_s}{dt} + M \frac{di_p}{dt}. \tag{31}$$

From (2) and (31) the rate of i_p and i_s when $i_e > i_s > 0$ are worked out as

$$\frac{di_p}{dt} = \frac{1}{1-k^2}\frac{1}{L_p}\left(v_p - R_{p,eq} i_p\right) - \frac{k^2}{1-k^2}\frac{1}{M}\left(R_{Ls} + R_D\right) i_s \tag{32}$$

$$\frac{di_s}{dt} = \frac{k^2}{1-k^2}\frac{1}{M}\left(v_p - R_{p,eq} i_p\right) - \frac{1}{1-k^2}\frac{1}{L_s}\left(R_{Ls} + R_D\right) i_s. \tag{33}$$

If $-i_e < i_s < 0$ the four-diode conduction is enables as well and, consequently, v_s is still given by (30). Hence, (32) and (33) hold also in this operating condition.

The expression relevant to the current i_e is found by substituting (8) in (29). It is

$$\frac{di_e}{dt} = -\frac{2V_D}{L_e} - \frac{R_e + R_D}{L_e} i_e \tag{34}$$

and obviously results to be independent from i_s.

III. CURRENT QUALITATIVE ANALYSIS

The aim of this Section is to fix in the supply period of the HFRT a time instant suitable to be used as initial point for the quantitative analysis of the currents that will be reported in the next Section.

The first step in the qualitative analysis of the HFRT is recognizing that proper operation of the excitation coil requires i_e to be continuous and nearly constant. On the other hand, supplying the excitation coil through a rotary transformer entails that both i_p and i_s have a predominant alternate component. Consequently, i_s must cross the zero value while i_e is close to its nominal value. This condition is inherent to the functioning of the system and happens irrespectively from its actual parameters. After this crossing point, the general functioning of the system is derived from the equations worked out in the previous Section.

A. DR OPERATIONS AFTER i_s ZERO CROSSING

In a time interval around the zero crossing of i_s the condition $|i_s| < i_e$ is verified and consequently (32) and (33) hold. Exactly at the crossing instant, being $i_s = 0$, they change into

$$\frac{di_p}{dt} = \frac{1}{1-k^2}\frac{1}{L_p}\left(v_p - R_{p,eq} i_p\right) \tag{35}$$

$$\frac{di_s}{dt} = \frac{k^2}{1-k^2}\frac{1}{M}\left(v_p - R_{p,eq} i_p\right). \tag{36}$$

Let us consider the positive zero crossing of i_s. It can actually happen only if di_s/dt is positive and hence, from (36), v_p must be equal to V_{dc}. Consequently, at the crossing instant, i_p is increasing as well and, if $M > L_s$, the rate of i_s is higher than the rate of i_p.

After the zero crossing and before i_s reaches i_e, the relations (32) and (33) hold with $v_p = V_{dc}$ so that the two currents keep on increasing even if with a decreasing rate. In the meantime, i_e decreases with the rate given by (34). This behavior carries on until i_s reaches the same value as i_e.

B. DR OPERATIONS AFTER i_s REACHES i_e

When the current i_s reaches i_e, the diodes D_1 and D_4 carry the current $i_s = i_e$ whilst D_2 and D_3 stop conducting. Then the system behavior is described by equations (12) and (13) with $v_p = V_{dc}$.

With respect to the situation described in the previous Subsection, $R_{s,eq}$ is slightly higher than $(R_{Ls} + R_D)$, $L_{s,eq}$ is much higher than L_s, and k_{eq}^2 is much lower than k^2. These conditions give the hint that di_s/dt and di_p/dt are still positive and that the two currents further increase even if at a rate much slower than before because the first terms in the right-hand side of (12) and (13) are lower than the ones of (32) and (33). Being $i_s = i_e$, the current in the excitation coil increases at the same rate as i_s. This behavior carries on until v_p switches to 0.

Neither the zero crossing of i_s nor its intersection with i_e are suitable starting points to perform a more depth analysis of the system functioning. Indeed, both of them happen after the switching of v_p from 0 to V_{dc}, with two delays that depend on all the system parameters and cannot be directly controlled.

C. DR OPERATIONS AFTER v_p SWITCHES TO 0

Let us assume that the two-diode conduction carries on even after the switching of v_p to 0. If this condition actually occurs, (13) still holds in the form

$$\frac{di_s}{dt} = -\frac{k_{eq}^2}{1-k_{eq}^2}\frac{1}{M} R_{p,eq} i_p - \frac{1}{1-k_{eq}^2}\frac{1}{L_{s,eq}}\left(2V_D + R_{s,eq} i_s\right). \tag{37}$$

The currents i_s and i_p, just after the switching can be considered the same as just before it. Consequently, the variation of the rate of i_s caused by the switching of the supply voltage, obtained from (13) with $v_p = 0$ and $v_p = V_{dc}$, results in

$$\Delta\frac{di_s}{dt} \triangleq \left.\frac{di_s}{dt}\right|_{v_p=0} - \left.\frac{di_s}{dt}\right|_{v_p=V_{dc}} = -\frac{k_{eq}^2}{1-k_{eq}^2}\frac{1}{M} V_{dc}. \tag{38}$$

Because of the switching of v_p, v_s is subjected to a variation as well. It is obtained from (16) in the form

$$\Delta v_s \triangleq v_s|_{v_p=0} - v_s|_{v_p=V_{dc}} = -\left(1 - \frac{k_{eq}^2}{k^2}\right)\frac{1}{1-k_{eq}^2}\frac{M}{L_p} V_{dc}. \tag{39}$$

From (10) and (8) and by the hypothesis that $i_s = i_e$ it comes that

$$\frac{di_e}{dt} = \frac{v_s}{L_e} - \frac{(2R_D + R_e)\, i_e}{L_e} - \frac{2V_D}{L_e}. \tag{40}$$

From the last one it derives that the variation of the rate of i_e is

$$\Delta\frac{di_e}{dt} = \frac{\Delta v_s}{L_e} = -\left(1 - \frac{k_{eq}^2}{k^2}\right)\frac{M}{L_p L_e}V_{dc}. \quad (41)$$

After some manipulations that involve the second of (14) and (15), (41) can be rewritten in the form

$$\Delta\frac{di_e}{dt} = -k_{eq}^2\frac{1}{M}V_{dc}. \quad (42)$$

Clearly (38) and (42) are different being the absolute value of the variation of di_s/dt higher than that one of di_e/dt. It means that after the switching of v_p the condition $i_s = i_e$ cannot be maintained because i_s would decrease quicker than i_e and become lower than this latter one. Consequently, the four-diode conduction takes place.

Then, the rates of i_s and i_p come respectively from (32) and (33) setting $v_p = 0$ and are

$$\frac{di_p}{dt} = -\frac{1}{1-k^2}\frac{1}{L_p}R_{p,eq}i_p - \frac{k^2}{1-k^2}\frac{1}{M}(R_{Ls}+R_D)\,i_s \quad (43)$$

$$\frac{di_s}{dt} = -\frac{k^2}{1-k^2}\frac{1}{M}R_{p,eq}i_p - \frac{1}{1-k^2}\frac{1}{L_s}(R_{Ls}+R_D)\,i_s. \quad (44)$$

The rate of i_e is given by (34). All the three currents decay toward zero, but i_s and i_p decreases much quicker than i_e because of the high value of k^2 and the values of M and L_s, which are much lower than L_e.

This operating condition carries on until v_s switches from 0 to $-V_{dc}$.

D. DR OPERATIONS AFTER v_p SWITCHES TO $-V_{dc}$

As demonstrated in the previous Subsection, just before v_p switches to $-V_{dc}$ the condition $i_s < i_e$ holds and i_s decreases quicker than i_e.

After v_p switches to $-V_{dc}$, (32) and (33) change into

$$\frac{di_p}{dt} = -\frac{1}{1-k^2}\frac{1}{L_p}\left(V_{dc} + R_{p,eq}i_p\right) - \frac{k^2}{1-k^2}\frac{1}{M}(R_{Ls}+R_D)\,i_s \quad (45)$$

$$\frac{di_s}{dt} = -\frac{k^2}{1-k^2}\frac{1}{M}\left(V_{dc} + R_{p,eq}i_p\right) - \frac{1}{1-k^2}\frac{1}{L_s}(R_{Ls}+R_D)\,i_s. \quad (46)$$

and i_s decreases even faster. At the same time, the condition $i_s < i_e$ is maintained. The rectifier carries on operating in this condition until the negative crossing of i_s. Then the conduction diodes changes from the pair D_1, D_4 to the pair D_2, D_3. From here on, the currents continue to decrease in a symmetrical way with respect to the description given in Subsection III-A.

The time instants of the switching of v_p to 0 or to $-V_{dc}$ are fixed only by the switching period and the phase shift of the HFI. Consequently, both of them can profitably be used as starting points for a quantitative analysis of the system operations. From this point of view, the switching of v_p to 0 is more advantageous because it corresponds to the maximum of i_e whilst the minimum of i_e is reached with a delay with respect to the switching of v_p to $-V_{dc}$.

IV. CURRENT QUANTITATIVE ANALYSIS

This Section uses the results of the previous one to work out analytical expressions of the currents in the different working conditions of the system. The aim of this activity is finding the relations that link the system parameters to the values of the currents in some particular time instants, such as the ones corresponding to their peak values. In performing the analysis, some simplifications are introduced in order to obtain closed form results.

A. CURRENTS AFTER v_p SWITCHES TO 0

Let us set origin t_0 for the time reference at the switching instant of v_p from V_{dc} to 0, as shown in Fig. 5. The values of the currents at $t_0 = 0$ are denoted as i_{p0}, i_{s0}, and i_{e0}, with $i_{s0} = i_{e0}$ as demonstrated in the previous Section. Integration of (44) and (34) would give exponential expressions for the two currents. In order to make easier the analysis of the system, the rates of the currents are approximated by constants equal to their values at t_0. This assumption corresponds to substitute i_{s0} for i_s in (44) and i_{e0} for i_e in (34).

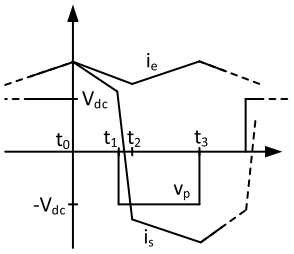

FIGURE 5. Qualitative waveforms of I_s and i_e.

According to this simplification, at the time instant

$$t_1 = t_0 + (1-2\delta)\frac{T}{2} = (1-2\delta)\frac{T}{2}, \quad (47)$$

i.e., when v_p switches from 0 to $-V_p$, the currents reach the approximate values given by

$$i_{s1} = i_{s0} - \left[\frac{k^2}{1-k^2}\frac{1}{M}R_{p,eq}i_{po} + \frac{1}{1-k^2}\frac{1}{L_s}(R_{Ls}+R_D)\,i_{so}\right](1+-2\delta)\frac{T}{2} \quad (48)$$

$$i_{e1} = i_{e0} - \left(\frac{2V_D}{L_e} + \frac{R_e+R_D}{L_e}i_{e0}\right)(1-2\delta)\frac{T}{2}. \quad (49)$$

B. CURRENTS AFTER v_p SWITCHES TO $-V_{dc}$

After the switching of v_p to $-V_{dc}$ the rate of i_s is given by (46). In this case, an approximation can be done by considering only the effect of V_{dc} whilst neglecting the effects of the resistances.

Under this approximation, the current i_s decreases according to

$$i_s = i_{s1} - \frac{k^2}{1-k^2}\frac{1}{M}V_{dc}\,(t-t_1)\,, \tag{50}$$

crosses the zero and then keeps decreasing with the same rate until it reaches -i_e.

In the meantime, i_e decrease with the same rate considered to obtain (49), and is approximated by

$$i_e = i_{e1} - \left(\frac{2V_D}{L_e} + \frac{R_e + R_D}{L_e} i_{e0}\right)(t-t_1)\,. \tag{51}$$

The current i_s reaches -i_e at the time instant t_2, after a time interval equal to

$$\Delta t \triangleq t_2 - t_1 = \frac{i_{s1} + i_{e1}}{\frac{k^2}{1-k^2}\frac{1}{M}V_{dc} + \frac{2V_D}{L_e} + \frac{R_e+R_D}{L_e} i_{e0}}, \tag{52}$$

obtained equating (50) to the opposite of (51).

The complexity of (52) makes it difficult to be used in the subsequent analysis. However, Δt can be approximated by

$$\Delta t \cong \frac{2i_{e0}}{\frac{k^2}{1-k^2}\frac{1}{M}V_{dc} + \frac{2V_D}{L_e} + \frac{R_e+R_D}{L_e} i_{e0}}, \tag{53}$$

obtained by considering that i_e is nearly constant so that i_{e1} can be approximated by i_{e0}, and by neglecting the difference between i_{s1} and $i_{s0} = i_{e0}$.

At $t = t_2$, i_e reaches its minimum value

$$i_{e2} = i_{e1} - \left(\frac{2V_D}{L_e} + \frac{R_e + R_D}{L_e} i_{e0}\right)\Delta t \tag{54}$$

whilst i_s keeps decreasing even after t_2 with a different slope.

C. CURRENTS AFTER i_s REACHES -i_e

After i_s reaches -i_e, its evolution carries on in a symmetrical way with respect to the analysis performed in Subsection III-B. The condition i_s = -i_e is maintained and the two current vary with opposite rates. The rate of i_s, given by (13) with v_p = -V_{dc}, is still negative but its absolute value is much smaller than in the previous condition. Instead, the rate of i_e, according to (22), is positive being opposed to that of i_s, thus confirming that i_e reached its minimum value at $t = t_2$. Expression (13) can be simplified by neglecting the voltage drop across $R_{p,eq}$ with respect to -V_{dc} so that at the time instant $t_3 = T/2$, when v_p switches back to 0, i_e is approximated as

$$i_{e3} = i_{e2} + \left[\frac{k_{eq}^2}{1-k_{eq}^2}\frac{1}{M}V_{dc} + \frac{1}{1-k_{eq}^2}\frac{1}{L_{s,eq}}\left(2V_D + + R_{s,eq} i_{e0}\right)\right] \times (\delta T - \Delta t)\,. \tag{55}$$

At t_3 it is $i_{e3} = i_{e0}$. Using (49), (54), and (55), this relation can be rewritten in the form

$$-\left(\frac{2V_D}{L_e} + \frac{R_e + R_D}{L_e} i_{e0}\right)\left((1-2\delta)\frac{T}{2} + \Delta t\right) + \frac{1}{1-k_{eq}^2}\left[\frac{k_{eq}^2}{M}V_{dc} + -\frac{2V_D}{L_{s,eq}} - \frac{R_{s,eq}}{L_{s,eq}} i_{e0}\right](\delta T - \Delta t) = 0. \tag{56}$$

If Δt is neglected with respect to the other time intervals, i_{e0} is easily found by solving (56) with $\Delta t = 0$ obtaining

$$i_{e0} = \frac{\frac{1}{1-k_{eq}^2}\left(k_{eq}^2\frac{1}{M}V_{dc} - \frac{2V_D}{L_{s,eq}}\right)\delta T - \frac{2V_D}{L_e}(1-2\delta)\frac{T}{2}}{\frac{R_e+R_D}{L_e}(1-2\delta)\frac{T}{2} + \frac{1}{1-k_{eq}^2}\frac{R_{s,eq}}{L_{s,eq}}\delta T}. \tag{57}$$

By exploiting the approximations $R_{s,eq} \approx R_e$, R_e+$R_d \approx R_e$, and $L_{s,eq} \approx L_e$, (57) is rewritten as

$$i_{e0} = \frac{\frac{k_{eq}^2}{1-k_{eq}^2}\frac{L_e}{R_e}\frac{1}{M}V_{dc}\delta}{(1-2\delta)\frac{1}{2} + \frac{1}{1-k_{eq}^2}\delta} - \frac{2V_D}{R_e}. \tag{58}$$

Otherwise, using expression (53) for Δt, a more accurate approximation of i_{e0} is obtained from (56) by solving the second-degree equation

$$a i_{e0}^2 + b i_{e0} + c = 0 \tag{59}$$

whose coefficients are given by (A1)-(A3) in the appendix. Generally, (59) has two solutions and both of them could be positive. In this case, the solution to be selected to approximate i_{e0} is the one with the lower absolute difference with respect to (57).

Once i_{e0} has been obtained from (57), (58), or (59), i_{e1} is easily obtained from (49) and i_{e2} from (54) using (53).

D. DETERMINATION OF i_p AND i_s

According to the analysis performed in Sections III-A and III-B, it is $i_{s0} = i_{e0}$, so that it is possible to work out i_{p1} by

$$i_{p1} = i_{p0} - \left(\frac{1}{1-k^2}\frac{1}{L_p}R_{p,eq} i_{p0} + \frac{k^2}{1-k^2}\frac{1}{M}(R_{Ls}+R_D)\, i_{s0}\right) \times (1 + -2\delta)\frac{T}{2}, \tag{60}$$

obtained from (32) approximating i_p with i_{p0} and i_s with i_{s0} in the time interval (t_0, t_1) and remembering that in this interval $v_p = 0$.

In the time interval (t_1, t_2), while i_s switches from i_e to -i_e, (32) still holds and i_s is about symmetrical with respect to the zero value so that the time integral of the second term on the right-hand side of (32) is small. Moreover, now v_p = -V_{dc} and its contribution to the variation of i_p is much larger than the one due to the resistive drops across $R_{p,eq}$ and (R_{Ls}+R_D). Consequently, the following expression can be written.

$$i_{p2} = i_{p1} - \frac{1}{1-k^2}\frac{1}{L_p}V_{dc}\Delta t. \tag{61}$$

After i_s reached $-i_e$, in the time interval (t_2, t_3) i_p evolves according to (19) with $v_p = -V_{dc}$. At $t = t_3$, i_p is equal to $-i_{p0}$ and is approximated as

$$i_{p3} = -i_{p0} = i_{p2} + \left[\frac{1}{1-k_{eq}^2} \frac{1}{L_p} \left(-V_{dc} + R_{p,eq} i_{p0}\right) + \frac{k_{eq}^2}{1-k_{eq}^2} \frac{1}{M} \left(2V_D + R_{s,eq} i_{s0}\right) \right] (\delta T - \Delta t), \quad (62)$$

where i_p and i_s have been substituted for by $-i_{s0}$ and $-i_{p0}$ because in the considered time interval both of them are near to their negative peak value.

Substituting (60) in (61) and then using the obtained expression of i_{p2} in (62) allows to work out i_{p0} in the form

$$i_{p0} = \frac{i_{p0,vp} + i_{p0,is0} - \frac{k_{eq}^2}{1-k_{eq}^2} \frac{1}{M} (\delta T - \Delta t)\, 2V_D}{2 + \frac{R_{p,eq}}{L_p} \left(-\frac{1}{1-k^2} (1-2\delta) \frac{T}{2} + \frac{1}{1-k_{eq}^2} (\delta T - \Delta t) \right)}, \quad (63)$$

where the terms $i_{p0,vp}$ and $i_{p0,is0}$ accounts for the contributions of v_p and of i_{s0}, respectively. They are given by

$$i_{p0,vp} = \frac{1}{L_p} \left[\frac{1}{1-k^2} \Delta t + \frac{1}{1-k_{eq}^2} (\delta T - \Delta t) \right] V_{dc} \quad (64)$$

and

$$i_{p0,is0} = \frac{1}{M} \left[\frac{k^2}{1-k^2} (R_{Ls} + R_D) (1-2\delta) \frac{T}{2} - \frac{k_{eq}^2}{1-k_{eq}^2} R_{s,eq} (\delta T + -\Delta t) \right] i_{s0}. \quad (65)$$

Once i_{p0} is worked out, it can be inserted in (48) to find i_{s1}. Then the analysis can be concluded quickly by using (60) and (61) con obtain i_{p1} and i_{p2} and by remembering that i_{e2} is equal to i_{s2}, obtained from (54).

The results obtained from the previous equations are obviously approximations of the actual values. In [16] the approximation error is reduced by suitable tuning coefficients. In this paper, a better approximation of the current's values is obtained by an iterative procedure that uses i_{s1} obtained from (48) and i_{e1} coming from (49) to assess a more accurate value of Δt, by means of (52), and of i_{e0} by solving (56) obtaining (66), as shown at the bottom of the page.

The new value of i_{e0} is used in (49) to update i_{e1} and the new value of i_{p0}, given by (63), is used again in (48) to update i_{s1}. Then the procedure starts again from (52) computing a new value of Δt. It is repeated until the obtained results converge to stable values. The analysis of the waveforms of the currents involved in the functioning of the rotary transformer is completed by computing i_{p1} and i_{p2} by (60) and (61) and $i_{e2} = -i_{s2}$ by (54). The flowchart of the iterative procedure is reported in Fig. 6.

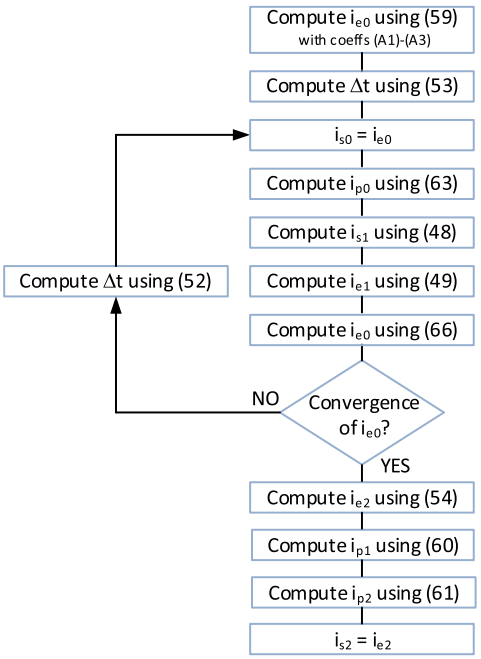

FIGURE 6. Flowchart for currents computation.

V. VALIDATION BY SIMULATION

The results obtained in the previous Sections have been verified by simulations performed in the Matlab-Simulink environment. The model used for the simulations has the parameters listed in Tab. 1. They are taken from a prototypal setup used for the experiments described in the next Section. A number of simulations have been performed with different values of δ and the amplitudes of the currents i_p, i_s, and i_e have been acquired at the time instant t_0, t_1, t_2 once the system reached the steady state. In Fig. 7, the values of i_{e0} and i_{e2} obtained from the simulation are highlighted by the blue circles and the red stars, respectively, whilst the same quantities computed using the equations worked out in the previous Sections are plotted using the solid blue line and the dashed red line.

Given the high value of L_e, i_e is nearly constant and, hence the difference between i_{e0} and i_{e2} is very small. For this reason, the series of circles ad stars appear superimposed and

$$i_{e0} = \frac{-\frac{2V_D}{L_e} \left[(1-2\delta) \frac{T}{2} + \Delta t \right] + \frac{1}{1-k_{eq}^2} \left[\frac{k_{eq}^2}{M} V_{dc} - \frac{2V_D}{L_{s,eq}} \right] (\delta T - \Delta t)}{\frac{R_e + R_D}{L_e} \left[(1-2\delta) \frac{T}{2} + \Delta t \right] + \frac{1}{1-k_{eq}^2} \frac{R_{s,eq}}{L_{s,eq}} (\delta T - \Delta t)} \quad (66)$$

TABLE 1. Prototype parameters.

Symbol	Meaning	Value
L_p	Primary coil inductance	23.5 µH
L_s	Secondary coil inductance	4.6 µH
M	Mutual inductance	7.3 µH
L_e	Excitation coil inductance	15 mH
R_p	Primary coil resistance	30 mΩ
R_s	Secondary coil resistance	10 mΩ
R_e	Excitation coil resistance	2.0 Ω
V_{dc}	Dc bus supply voltage	130 V
R_T	MOSFETs on-resistance	100 mΩ
R_D	Diodes on resistance	250 mΩ
V_D	Diodes on voltage	0.8 V
T	Supply period	11.8 µs
f	Supply frequency	85 kHz
g	Airgap	0.4 mm
D_{ext}	External diameter	35.0 mm
w_{back}	Width of the back ferrite	3.0 mm
w_{fe1}	Width of the inner ferrite	5.0 mm
wf_{e2}	Width of the outer ferrite	2.5 mm
h_{slot}	Total height of the core	16.4 mm
h_p	Height of the primary slot	8.0 mm
h_s	Height of the secondary slot	8.0 mm

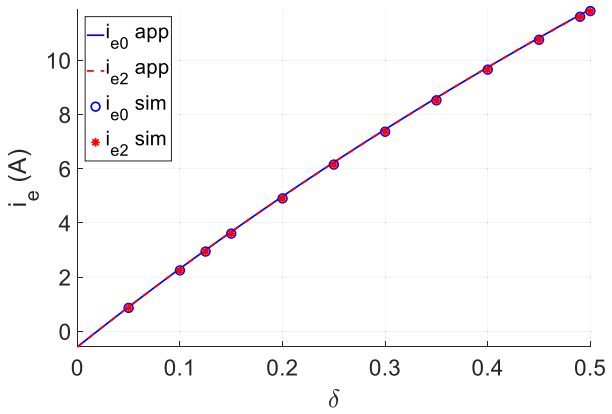

FIGURE 7. Simulated and approximated values of i_{e0} and i_{e2}.

the same happens with the two lines. It is more important to notice that the lines and the marks correspond nearly perfectly, thus demonstrating the accuracy of the results coming from the analytical approximation.

This accuracy is confirmed by Fig. 8, which reports the absolute and the relative errors between the results coming from the simulation and those worked out analytically. The figure shows that the percentual error is less than 2% when $\delta > 0.1$ and never exceeds 4%. Even in the worst case, the absolute error is less than 0.1 A.

Given the equalities $i_{s0} = i_{e0}$ and $i_{s2} = -i_{e2}$, these good performances are confirmed by Fig. 9, relevant to i_{s0}, i_{s1} and i_{s2}. The approximation of i_{s1}, instead, is not so good, and indeed the green crosses in Fig. 9 do not superimpose perfectly with the dotted green line. The absolute and relative errors relevant to i_{s0}, i_{s1} and i_{s2} are reported in Fig. 10. This figure shows that the maximum absolute error is of about 0.4 A and that it happens when $\delta = 0.2$. For smaller values of

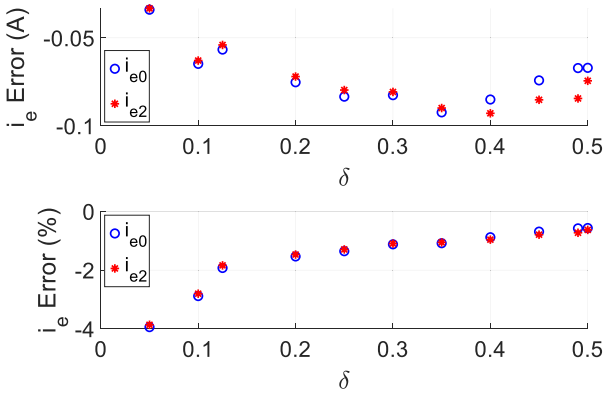

FIGURE 8. Absolute and relative errors on i_{e0} and i_{e1}.

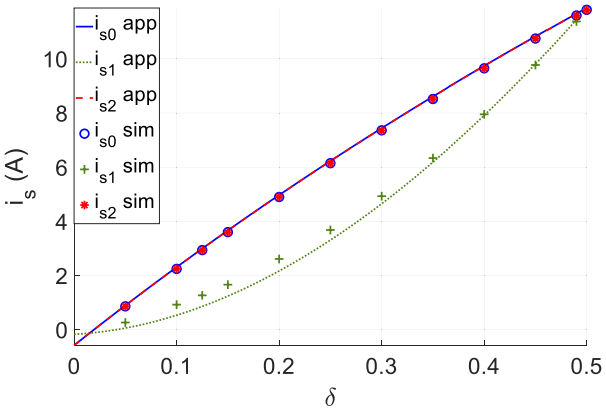

FIGURE 9. Simulated and approximated values of i_{s0} and i_{s1} and i_{s2}.

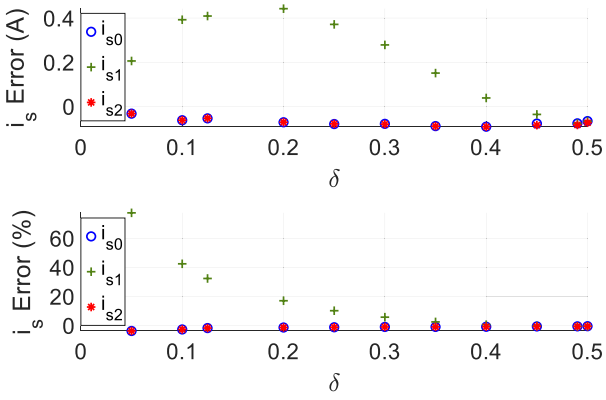

FIGURE 10. Absolute and relative errors on i_{s0} and i_{s1} and i_{s2}.

δ the absolute error decreases but the relative one increases and reaches the values of about 80% when $\delta = 0.05$. The corresponding absolute error is of 0.2 A.

Like it happens with i_s, Fig. 11 shows that the approximations of i_{p0} and i_{p2} are good whilst the approximation of i_{p1} is less accurate. Indeed, the green crosses are not superimposed to the dotted green line. Nevertheless, analysis of the absolute and relative errors plotted in Fig. 12 reveals

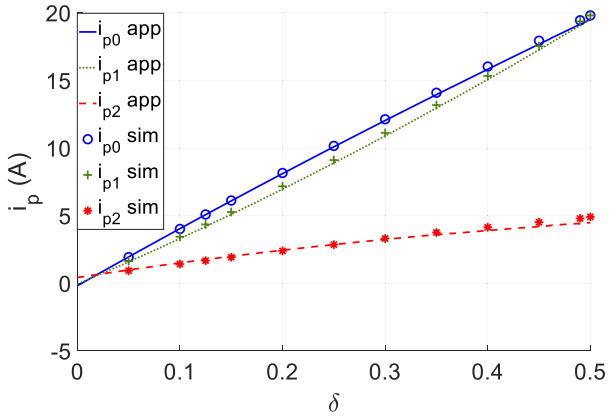

FIGURE 11. Simulated and approximated values of i_{p0} and i_{p1} and i_{p2}.

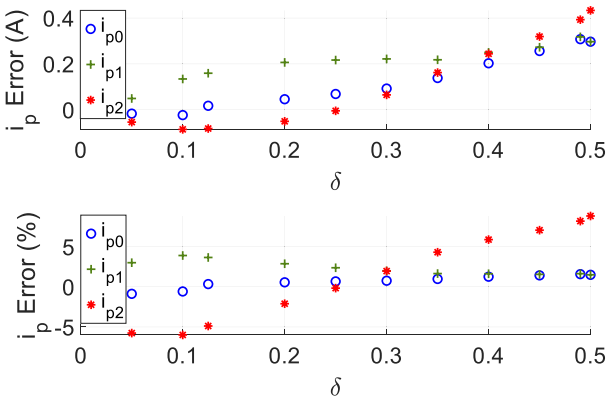

FIGURE 12. Absolute and relative errors on i_{p0} and i_{p1} and i_{p2}.

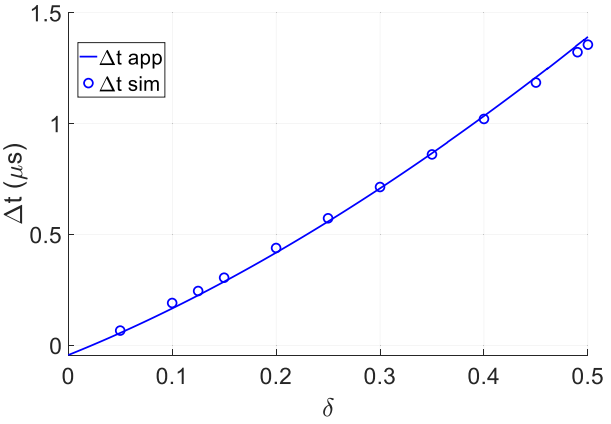

FIGURE 13. Simulated and approximated values of Δt.

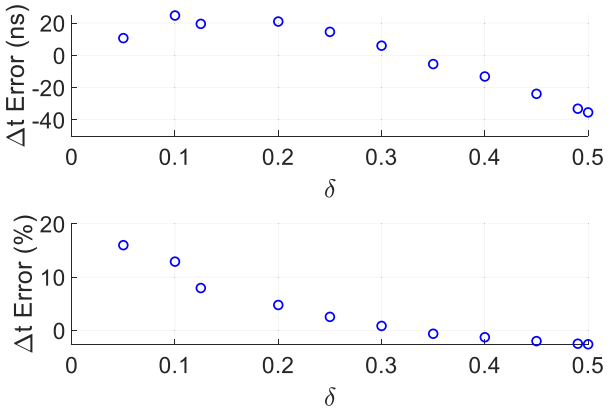

FIGURE 14. Absolute and relative errors on Δt.

that i_p is approximated much more accurately than i_s. Indeed, the absolute and relative errors on i_{p0} and i_{p2} are comparable with those on i_{e0} and i_{e2}, which are very small. The errors on i_{p1} are much smaller than those relevant to i_{s1}. The maximum absolute error on i_{p1} is a little more than 0.2 A and happens when $\delta = 0.3$ whilst the maximum relative error is less than 5% and happens when $\delta = 0.1$.

Beside the currents, the procedure described by Fig. 6 gives an approximation of Δt. It is reported in Fig. 13 and compared with the values coming from the simulations. Also in this case, the approximated values match satisfactory with those obtained by simulation. Fig. 14, which reports the approximation absolute and relative errors confirms the obtained accuracy.

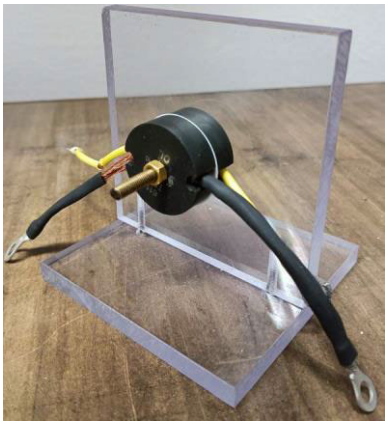

FIGURE 15. Prototypal HFRT.

VI. EXPERIMENTAL VALIDATION

The prototypal HFRT, shown in Fig. 15, has the geometrical layout given in Fig. 16. The windings of the primary and secondary coils are wounded into two cup cores that are faced each to the other through the airgap g. The dimensions of the cores are listed in Tab. 1. In order to effectively carry out its functions, the HFRT must be installed on a EESM with a configuration that could be similar to one of the two shown in Fig. 17. According to the layout on the left, the core of the secondary side is fitted into the shaft through the hole in the central column. The solution on the right, instead, shows the core of the secondary side inserted into a socket drilled in the shaft. The first layout is good from a thermal point of view because it helps to cool the core, while the second is better from a structural point of view.

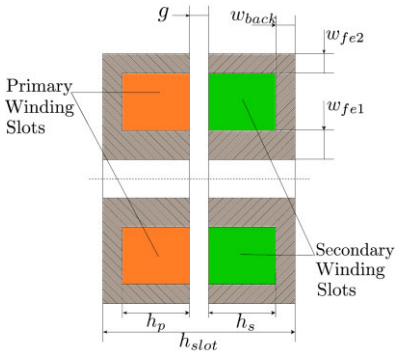

FIGURE 16. Sketch of the HFRT layout.

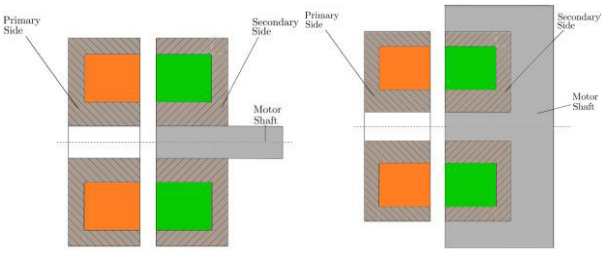

FIGURE 17. Sketch of the HFRT installed on an EESM.

During the experimental tests, the HFRT has been supplied by an HFI available in the lab. The HFI was designed to supply the transmitting coil of a wireless power transfer system [17] and is built around the SiC-MOSFET module CCS050M12CM2 from Cree [18] that now is out of production. A module with about the same characteristics has a bulk price of about 317 Euro. For the considered application, this module has oversized voltages and currents so that for an industrial realization of the HFI different power switches could be selected. By selecting six discrete SiC-MOSFETs from the price-list of an on-line seller, the price of the power section of the HFI could decrease to about 21 Euros. The total cost of the cores and of the Litz wire used to build up the HFRT resulted of 11.5 Euros.

During the tests, the voltages and currents relevant to the primary and secondary coils have been acquired by means suitable probes connected to a digital oscilloscope The voltage waveforms relevant to one of the tests are reported in the upper half of Fig. 18 whilst the lower half of the figure shows the currents.

According to Fig. 3, the voltage v_p cannot be acquired, instead, the voltage v_{AB} at the HFI output downstream the MOSFETs on-resistances R_T is reported. Because of the voltage drop across the latter resistances, the magnitude of v_{AB} decreases a little while the magnitude of i_p increases. The figure shows that v_s is subjected to a ringing phenomenon due to the resonance between the secondary coil inductance L_s and the parasitic capacitances of the diodes that form the DR.

The effects of the parasitic capacitances of the diodes and of the MOSFETs are recognized in the waveforms of the currents as well. Indeed, both i_p, drawn with the solid blue

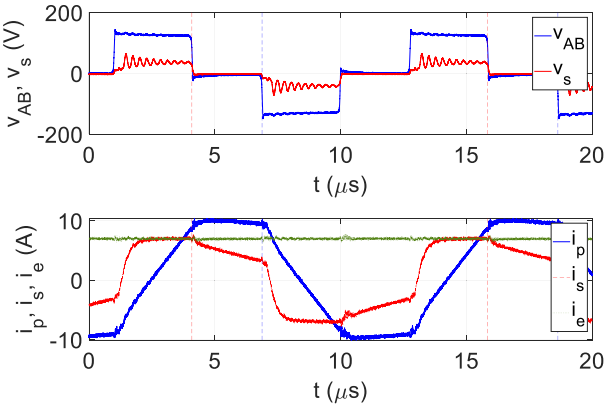

FIGURE 18. Primary and secondary voltages and currents.

line, and i_s, denoted by the dashed red line, exhibit smooth transitions between one operating condition and the other so that the cusps corresponding to the time instants t_0, t_1, and t_2 are not easily recognized.

The approximated values of the currents at the time instants t_0, t_1 and t_2 have been computed using the procedure described in Fig. 6, considering the parameters of Tab. 1 and the duty cycle obtained by processing the v_p waveform. The approximated values of the three currents at the time instants t_0, t_1, and t_2 are plotted in Fig. 19 using the circle to mark i_p, the triangle for i_s, and the cross for i_e. In order to make easier the analysis of the figure, the samples of the experimental currents have been filtered by a low pass filter having cutoff frequency equal to 200 times the supply frequency. The figure shows that the approximated values computed at t_0 and t_1 match satisfactory with the current waveforms and that most of the difference between the approximated and the experimental values is due to the smooth behavior of the latter ones. Being i_e nearly constant, it results unaffected by the parasitic capacitances and, indeed, the matching of the approximated values with the experimental ones is very good in all the three time instants. The difference between the two sets of values

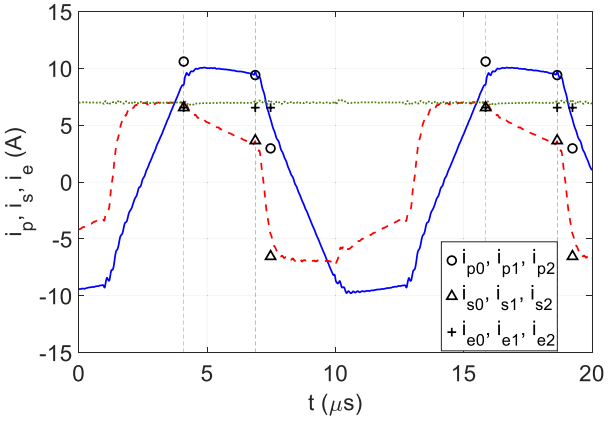

FIGURE 19. Primary and secondary currents with nominal airgap.

is due to the parasitic resistances of the connectors and cables that links the HFRT to the DR and that should be summed to R_D and R_e.

The test has been repeated after increasing the airgap between the two cores of the HFRT from 0.4 mm to 1.0 mm. In this new condition, some parameters of the HFRT changes as reported in Tab. 2. The corresponding experimental waveforms and approximated currents are plotted in Fig. 20. Also in this case, the correspondence between the approximated and the experimental current is, in general, satisfactory. If only i_e is considered, the correspondence is quite good.

TABLE 2. Prototype parameters with increased airgap.

Symbol	Meaning	Value
L_p	Primary coil inductance	14.3 µH
L_s	Secondary coil inductance	2.9 µH
M	Mutual inductance	3.8 µH
g	Airgap	1.0 mm

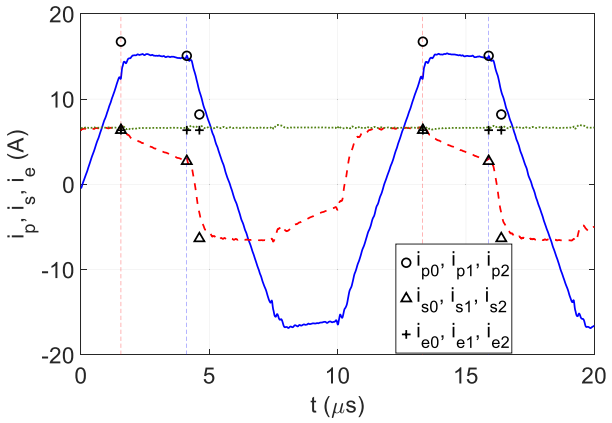

FIGURE 20. Primary and secondary currents with increased airgap.

As a final test, the efficiency of the HFRT with nominal airgap was evaluated. For this purpose, the average power delivered by the transformer over a supply period, computed from its secondary current and voltage, was divided by the average absorbed power, computed by processing the primary voltage and current. The difference between the second and the fist quantity gives the transformer losses. The efficiency and the power losses turned out to be about 92% and about 5 W, respectively.

VII. CONCLUSION

The paper presented an analytical model of a rotary transformed used to supply the excitation coil of a synchronous motor. All the steps followed in developing the model have been carefully analyzed and justified. The result of this activity is a procedure that allows to assess the values of the currents flowing in the transformer's coils and in the excitation coil as a function of the transformer and excitation coil parameters and of the supply voltage. In order to obtain closed form expressions of the currents, the presented model does not account for the parasitic capacitances of the supply inverter and of the diode rectifier. Nevertheless, it is able to work out the current values with satisfactory accuracy despite the non-idealities of the power converters connected to the transformer.

APPENDIX

The coefficients of (59) are

$$a = -\frac{R_e + R_D}{L_e}\left[(1-2\delta)\,\frac{T}{2}\,\frac{R_e + R_D}{L_e} + 2\right] + -\frac{1}{1-k_{eq}^2}\,\frac{R_{s,eq}}{L_{s,eq}}\left(\delta T\,\frac{R_e + R_D}{L_e} - 2\right) \tag{A1}$$

$$b = -\frac{2V_D}{L_e}\left[(1-2\delta)\,\frac{T}{2}\,\frac{R_e + R_D}{L_e} + 2\right] - (1 + -2\delta)\,\frac{T}{2}\,\frac{R_e + R_D}{L_e}\left(\frac{k^2}{1-k^2}\,\frac{1}{M}\,V_{dc} + \frac{2V_D}{L_e}\right) + \frac{1}{1-k_{eq}^2}\left(\frac{k_{eq}^2}{M}\,V_{dc} + -\frac{2V_D}{L_{s,eq}}\right)\left(\delta T\,\frac{R_e + R_D}{L_e} - 2\right) - \delta T\,\frac{1}{1-k_{eq}^2}\,\frac{R_{s,eq}}{L_{s,eq}}\left(\frac{k^2}{1-k^2}\,\frac{1}{M}\,V_{dc} + \frac{2V_D}{L_e}\right) \tag{A2}$$

$$c = \left(\frac{k^2}{1-k^2}\,\frac{1}{M}\,V_{dc} + \frac{2V_D}{L_e}\right)\left[-(1-2\delta)\,\frac{T}{2}\,\frac{2V_D}{L_e} + \delta T\,\frac{1}{1-k_{eq}^2}\left(\frac{k_{eq}^2}{M}\,V_{dc} - \frac{2V_D}{L_{s,eq}}\right)\right] \tag{A3}$$

REFERENCES

[1] D. S. Yadav and M. Manisha, "Electric propulsion motors: A comparative review for electric and hybrid electric vehicles," in *Proc. IEEE Int. Conf. Distrib. Comput. Electr. Circuits Electron. (ICDCECE)*, Ballari, India, Apr. 2022, pp. 1–6, doi: 10.1109/ICDCECE53908.2022.9793099.

[2] A. Krings and C. Monissen, "Review and trends in electric traction motors for battery electric and hybrid vehicles," in *Proc. Int. Conf. Electr. Mach. (ICEM)*, Gothenburg, Sweden, Aug. 2020, pp. 1807–1813, doi: 10.1109/ICEM49940.2020.9270946.

[3] Y. Kano, "Design optimization of brushless synchronous machines with wound-field excitation for hybrid electric vehicles," in *Proc. IEEE Energy Convers. Congr. Expo. (ECCE)*, Montreal, QC, Canada, Sep. 2015, pp. 2769–2775, doi: 10.1109/ECCE.2015.7310048.

[4] S. Saha and K. Mukherjee, "An asynchronous exciter fed brushless wound field synchronous motor drive for electrified vehicle application," in *Proc. Int. Conf. Power, Instrum., Control Comput. (PICC)*, Thrissur, India, Apr. 2023, pp. 1–6, doi: 10.1109/PICC57976.2023.10142883.

[5] V. Dmitrievskii, V. Prakht, and V. Kazakbaev, "Traction synchronous machine with rotor field winding and controlled magnetic anisotropy," in *Proc. Int. Conf. Ind. Eng., Appl. Manuf. (ICIEAM)*, vol. 81, Sochi, Russia, May 2024, pp. 512–517, doi: 10.1109/icieam60818.2024.10553881.

[6] Z. Zhang, "Robust stator-excited brushless synchronous machine: An attractive permanent magnet-free option," in *Proc. 22nd Int. Conf. Electr. Mach. Syst. (ICEMS)*, vol. 39, Harbin, China, Aug. 2019, pp. 1–6, doi: 10.1109/icems.2019.8921792.

[7] D. Talebi, M. C. Gardner, S. M. Seyedi, and H. A. Toliyat, "An asynchronously excited brushless wound field synchronous machine," in *Proc. Int. Conf. Electr. Mach. (ICEM)*, Valencia, Spain, Sep. 2022, pp. 2107–2113, doi: 10.1109/ICEM51905.2022.9910953.
[8] R. Manko, M. Vukotić, D. Makuc, D. Vonč ina, D. Miljavec, and S. Čorović, "Modelling of the electrically excited synchronous machine with the rotary transformer design influence," *Energies*, vol. 15, no. 8, p. 2832, Apr. 2022. [Online]. Available: https://www.mdpi.com/1996-1073/15/8/2832
[9] M. Tosi, "Rotary transformer design for brushless electrically excited synchronous machines," Ph.D. dissertation, Dept. Dipartimento di Ingegneria Industriale, Universita' degli Studi di Padova, Padua, Italy, 2014.
[10] H. Krupp and A. Mertens, "Rotary transformer design for brushless electrically excited synchronous machines," in *Proc. IEEE Vehicle Power Propuls. Conf. (VPPC)*, Montreal, QC, Canada, Mar. 2015, pp. 1–6, doi: 10.1109/VPPC.2015.7353009.
[11] J. Tang, "Design and control of electrically excited synchronous machines for vehicle applications," Ph.D. dissertation, Dept. Elect. Eng., Chalmers Univ. Technol., Gothenburg, Sweden, 2021.
[12] V. Ruuskanen, M. Niemelaä, J. Pyrhoönen, S. Kanerva, and J. Kaukonen, "Modelling the brushless excitation system for a synchronous machine," *IET Electr. Power Appl.*, vol. 3, no. 3, p. 231, Jun. 2009, doi: 10.1049/iet-epa.2008.0079.
[13] L. Xie, X. Yuan, J. Wang, and P. Mellor, "Design optimization of a rotary transformer converter for the excitation of electric machines," in *Proc. IEEE Energy Convers. Congr. Expo. (ECCE)*, Nashville, TN, USA, Oct. 2023, pp. 5846–5852, doi: 10.1109/ecce53617.2023.10362639.
[14] A. Baehr and N. Parspour, "Novel analytical calculation method of a wireless power transfer system for an inductive electrically excited synchronous machine," in *Proc. IEEE Wireless Power Technol. Conf. Expo (WPTCE)*, San Diego, CA, USA, Jun. 2023, pp. 1–6, doi: 10.1109/wptce56855.2023.10216184.
[15] D. Maier, J. Kurz, and N. Parspour, "Contactless energy transfer for inductive electrically excited synchronous machines," in *Proc. IEEE PELS Workshop Emerg. Technol., Wireless Power Transf. (WoW)*, London, U.K., Jun. 2019, pp. 191–195, doi: 10.1109/WoW45936.2019.9030682.
[16] B. Berweiler and B. Ponick, "Current and average temperature calculation for electrically excited synchronous machines in case of contactless energy supply," in *Proc. Int. Conf. Electr. Mach. (ICEM)*, Gothenburg, Sweden, Aug. 2020, pp. 1730–1735, doi: 10.1109/ICEM49940.2020.9270863.
[17] G. Buja, M. Bertoluzzo, and K. N. Mude, "Design and experimentation of WPT charger for electric city car," *IEEE Trans. Ind. Electron.*, vol. 62, no. 12, pp. 7436–7447, Dec. 2015, doi: 10.1109/TIE.2015.2455524.
[18] *CCS050M12CM2 1.2kV, 25mΩ All-Silicon Carbide Six-Pack (Three Phase) Module C2M MOSFET and Z-RecTM Diode*. Accessed: Oct. 30, 2024. [Online]. Available: https://www.mouser.com/catalog/specsheets/Cree_CS050M12CM2.pdf

MANUELE BERTOLUZZO received the M.S. degree in electronic engineering from the University of Padova, Padua, Italy, in 1993, and the Ph.D. degree in industrial electronics and computer science, in 1997. Since 2015, he has been an Associate Professor with the Department of Industrial Engineering, University of Padova, and holds a lectureship on road electric vehicles and systems for automation. He is involved in the analysis and design of power electronics systems, especially for wireless charging of electric vehicle batteries.

NICOLA BIANCHI (Fellow, IEEE) received the M.Sc. and Ph.D. degrees in electrical engineering from the Department of Electrical Engineering, University of Padova, Padua, Italy, in 1991 and 1995, respectively. In 1998, he joined the Department of Electrical Engineering, University of Padova, where he has been a Full Professor of electrical machines, converters, and drives, since 2018. He is currently with the Electric Drive Laboratory, Department of Electrical Engineering, University of Padova. His teaching activity deals with the design methods of electrical machines, introducing the finite element analysis of the machines. He is the author and co-author of more than 250 scientific articles on electrical machines and drives and two international books on the same subject. His research interests include the field of design and control of electrical machines, especially for variable speed applications. In 2014, he became a Fellow Member of the IEEE Industry Application Society. He is a member of the Electric Machines Committee and the Electrical Drives Committee of the IEEE Industry Applications Society. He was a recipient of ten best paper awards. He was the Technical Program Chair of the IEEE Energy Conversion Congress and Exposition, in 2014.

FRANCESCO TRIPALDI (Member, IEEE) received the M.S. degree in aerospace engineering from the University of Padova, Italy. He is currently a Research Fellow with the Electric Drives Laboratory, University of Padova. His research interest includes the design of high-frequency rotary transformers for the excitation of electrically excited synchronous motors.

Open Access funding provided by 'Università degli Studi di Padova' within the CRUI CARE Agreement